Conference on Modelling Fluid Flow (CMFF'22)
The 18th International Conference on Fluid Flow Technologies
Budapest, Hungary, August 30 -September 2, 2022

EFFECTS OF STOKES NUMBER ON PARTICLE DEPOSITION IN PARTICLE-LADEN TURBULENT PIPE FLOWS

Bisrat WOLDE[1], Lee MORTIMER[2], Michael FAIRWEATHER[3]

[1] Corresponding Author. School of Chemical and Process Engineering, Faculty of Engineering and Physical Sciences, University of Leeds. Leeds LS2 9JT, United Kingdom. E-mail: pmbw@leeds.ac.uk
[2] School of Chemical and Process Engineering, Faculty of Engineering and Physical Sciences, University of Leeds. Leeds LS2 9JT, United Kingdom. E-mail: l.f.mortimer@leeds.ac.uk
[3] School of Chemical and Process Engineering, Faculty of Engineering and Physical Sciences, University of Leeds. Leeds LS2 9JT, United Kingdom. E-mail: m.fairweather@leeds.ac.uk

ABSTRACT

The ability to predict particle dispersion, interaction and deposition in pipes is of value in improving the transport and process efficiency of high concentration particulate flows. In this work, the settling and deposition behaviour of suspensions of dense particles in a cylindrical pipe has been studied using direct numerical simulation coupled with Lagrangian particle tracking, with the influence of Stokes number on deposition examined. Fully developed particle-laden pipe flows are first driven to a steady state with shear Reynolds number, $Re_\tau = 720$, and particle Stokes numbers, $St^+ = 5.55$ and 16.78, with the constant pressure gradient forcing term subsequently decreased until the onset of particle deposition. From the analysis performed, it can be concluded that particle deposition is sensitive to Stokes number. Particle dispersion function and mean displacement values are demonstrated to decrease considerably faster with time at the higher Stokes number. Particle migration towards the lower wall regions of the pipe also shows the formation of a bed for such particles, whilst over the same time period only dune-like structures are produced at the lower Stokes number. An analysis of the particle dynamics, carried out by examining probability density functions of particle velocities and positions, confirms these findings.

Keywords: Particle flows, DNS, LPT, Stokes number, particle deposition.

NOMENCLATURE

d_p^*	[-]	Particle diameter
D	[m]	Pipe inner diameter
$D_{y(t)}^*$	[-]	Dispersion function
$\underline{f_i}$	[-]	Flow forcing term
Fr	[-]	Froude number
g	[ms^{-2}]	Acceleration due to gravity
$\underline{\hat{g}}$	[-]	Unit vector in gravity direction
L	[m]	Characteristic length scale
N_p	[-]	Number of particles
p^*	[-]	Pressure in bulk units
r	[m]	Radial coordinate
R	[m]	Pipe radius
Re_b, Re_τ	[-]	Bulk and shear Reynolds number
St	[-]	Stokes number
Δt^*	[-]	Particle timestep
$\underline{u}^*$	[-]	Mean velocity in bulk units
$\underline{u}_p^*, \underline{u}_f^*$	[-]	Particle and fluid velocity vector
$\underline{u}_s^*$	[-]	Slip velocity
$\underline{u}_\tau$	[ms^{-1}]	Shear velocity
U_b	[ms^{-1}]	Bulk mean velocity
$\underline{x}_p^*$	[-]	Particle position vector
$y_{i(t)}^*$	[-]	Particle vertical position
$y_{m(t)}^*$	[-]	Particle vertical mean position
z	[m]	Axial position
θ	[-]	Azimuthal coordinate
μ	[Pa. s]	Dynamic viscosity
ν	[m$^2 s^{-1}$]	Kinematic viscosity
ρ	[kgm^{-3}]	Fluid density
ρ_f, ρ_s	[kgm^{-3}]	Density of fluid and solid phase
ρ_p^*	[-]	Particle-fluid density ratio
$\underline{\underline{\tau}}$	[Pa]	Fluid Stress tensor
ϕ	[-]	Volume fraction
$\underline{\omega}_f^*$	[-]	Vorticity of fluid

Abbreviations and Acronyms

CFD	Computational fluid dynamics
DNS	Direct numerical simulation
LPT	Lagrangian particle tracking/tracker
PDF	Probability density function
SEM	Spectral element method
x, y, z	Cartesian coordinates
*	Non-dimensional units

1. INTRODUCTION

Accurate simulation of multiphase turbulent flows is of fundamental importance in many industrial and scientific research applications. Additionally, the generation of understanding through accurate modelling of turbulent multiphase flows is valuable across numerous industries such as chemical engineering, agriculture and nuclear waste processing [1].

Very few direct numerical simulation (DNS) studies have been performed in the past to investigate turbulent pipe flows at moderately high Reynolds numbers ($\boldsymbol{Re_b}$ = 11,700), and even fewer with a particulate phase present. In the past, multiphase DNS investigations have used mainly one-way coupling between the particles and the fluid, and at low Reynolds numbers [2]. There is a noticeable absence of four-way coupled DNS-based work, particularly in cylindrical geometries. Further, no previous modelling studies have considered the onset of particle deposition in such flows. As computational power increases it is now possible to perform such fully coupled simulations. The effects of particles on the fluid and interparticle collisions in turbulent pipe flows at moderately high Reynolds numbers are therefore being investigated here, with the emphasis placed on the analysis of results to determine particle dispersion and particle deposition out of the flow to form solid beds.

In this work a predictive methodology was developed based on DNS coupled with Lagrangian particle tracking (LPT) to study the details of particle deposition at two different particle Stokes numbers, $St^+ = 5.55$ and 16.78. An openly available computational fluid dynamic (CFD) solver, Nek5000, has been utilised as the basis for the work reported [3]. The solver is based on the spectral element method (SEM) with a high order residual technique. It is favourable for its high spectral accuracy, parallel process scaling and low numerical dispersion and dissipation [4]. The DNS code has been further extended with a four-way coupled LPT code to allow for high fidelity simulation of depositing particle-laden pipe flows.

2. METHODOLOGY

2.1. Single-Phase Flow Simulations

To solve the descriptive CFD equations, the DNS solver Nek5000 was used, as developed by Fischer et al. [3]. This solver is based on the spectral element method, an efficiently parallelisable, high-order weighted residual technique with excellent accuracy, and low numerical dispersion and dissipation. The Navier-Stokes equations are solved in non-dimensional form. In this work, all simulations were performed under the assumption that the fluid was Newtonian. The system studied was a pressure-driven incompressible flow in a long straight pipe with circular cross-section and an internal diameter, D. The time-dependent non-dimensional Navier-Stokes equations are given as:

$$\underline{\nabla}.\underline{u}^* = 0 \tag{1}$$

$$\frac{\partial \underline{u}^*}{\partial t^*} + \left(\underline{u}^*.\underline{\nabla}\right)\underline{u}^* = -\underline{\nabla}p^* + \frac{1}{Re_b}\,\underline{\nabla}\cdot\underline{\underline{\tau}}^* + \underline{f_i} \tag{2}$$

Here, $\underline{u}^*\left(\underline{x}^*, t^*\right)$ is the fluid velocity vector, non-dimensionalised using the bulk velocity, U_b, with the position vector, $\underline{x}^*$, and time, t^*, non-dimensionalised as $\underline{x}^* = \underline{x}/D$ and $t^* = tU_b/D$, respectively. Also, p^* is the non-dimensionalised pressure term for high-velocity flow, $p^* = p/\rho U_b^2$. The bulk Reynolds number, Re_b, is defined as $Re_b = U_b D/\nu$, where ν is the fluid kinematic viscosity. $\underline{\underline{\tau}}^*$ is the non-dimensionalised fluid stress tensor, $\underline{\underline{\tau}}^* = \underline{\underline{\nabla u^*}} + \underline{\underline{\nabla u^{*T}}}$, and $\underline{f_i}$ is a forcing term representing the driving pressure gradient and the two-way interaction between the fluid and the particles.

Eqs. (1) and (2) are solved numerically using the spectral element method along with appropriate boundary conditions. In three-dimensional space, these equations are discretised as grid points by the Lagrange-Galerkin approximation method. Nth-order Lagrange polynomial interpolants on Gauss-Lobatto-Legendre points are implemented as a basis for velocity space and Lagrangian interpolants of order N-2 on Gauss-Legendre quadrature points are employed for pressure space. Resolution of the Kolmogorov length scale was confirmed.

Table 1. Fluid phase mesh parameters.

$\boldsymbol{Re_b}$	$\boldsymbol{Re_\tau}$	Elements	Grid Points
3975	277	36,576	18,726,912
11700	720	36,576	18,726,912

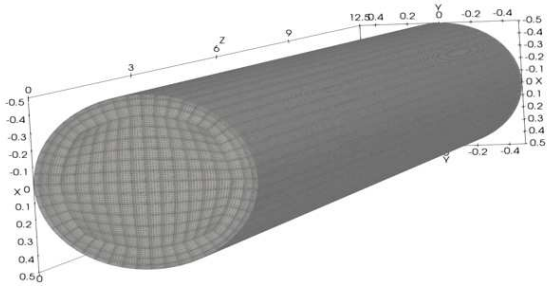

Figure 1. Computational mesh topology with Gauss-Lobatto-Legendre quadrature points (N = 7) for simulations at $Re_\tau = 277$ and $Re_\tau = 720$.

The computational domain consisted of a circular pipe of diameter, D, and length, $L = 12.5D$, partitioned into 36,576 spectral elements. Within the macro-elements the velocity field was represented by high-order tensor-product Gauss-Lobatto-Legendre

polynomial expansions of order N. The flow in the streamwise direction was forced by a constant pressure gradient. The shear Reynolds numbers based on the shear stress velocity considered below were $Re_\tau \approx 277$ and $Re_\tau \approx 720$. For both simulations, the same mesh topology and number of spectral elements was used. Gauss-Lobatto-Legendre quadrature points (N = 7) were used to distribute the vertices in each element [5]. The total number of elements and grid points used are given in Table 1 while Figure 1 illustrates the mesh topology implemented in all simulations.

2.2. Lagrangian Particle Tracking

The LPT solves a force-balance equation for each particle in the system, represented as an impenetrable computational sphere, under the assumption of point particles. The particle equations of motion for all forces considered in the multiphase flows are given below. In this research, a modified Maxey and Riley [6] equation was used. The non-dimensional form of the equations of motion for spherical particles, as implemented in the code, are:

$$\underline{u}_p^* = \frac{\partial \underline{x}_p^*}{\partial t^*} \tag{3}$$

$$\frac{\partial \underline{u}_p^*}{\partial t^*} = \frac{1}{M_{VM}} \left[\begin{array}{l} \frac{3C_D|\underline{u}_s^*|}{4d_p^*\rho_p^*}\underline{u}_s^* + \frac{1}{Fr}\left(1-\frac{1}{\rho_p^*}\right)\underline{\hat{g}} + \\ \frac{3C_L}{4\rho_p^*}(\underline{u}_s^* \times \underline{\omega}_f^*) + \frac{D'\underline{u}_f^*}{2\rho_p^* Dt^*} + \frac{D\underline{u}_f^*}{\rho_p^* Dt^*} \end{array} \right] \tag{4}$$

In Eqs. (3) and (4), $\underline{u}_p^*$ is the particle velocity vector, $\underline{x}_p^*$ the particle position vector, C_D the drag coefficient, and $\underline{u}_s^*$ the slip velocity given as $\underline{u}_f^* - \underline{u}_p^*$, where $\underline{u}_f^*$ and $\underline{u}_p^*$ are the fluid and particle velocity vectors, respectively. Also, d_p^* is the particle diameter, ρ_p^* the density ratio, Fr is the Froude number, which is defined as $Fr = u_b^2/gD$, where g is gravitational acceleration and $\underline{\hat{g}}$ is a unit vector in the direction of gravitational attraction, $\underline{\omega}_f^*$ is the vorticity of fluid which is given by $\underline{\omega}_f^* = \underline{\nabla} \times \underline{u}_f^*$, and the full equation is divided by $M_{VM} = (1 + 1/2\rho_p^*)$ to account for the virtual mass force. The particle bulk Stokes number is given as $St_b = d_p^{2^*}\rho_p^* Re_b/18$, and the shear Stokes number as $St^+ = d_p^{2^*}\rho_p^* Re_\tau^2/18$. A detailed explanation of these forces is provided by Mortimer et al. [7].

The drag force occurs due to movement through a resistive fluid phase and is a dominant force in the fluid-particle flow [8], while the lift force arises due to shear across the particle. Saffman [9] studied the strength and direction of the lift force for low particle Reynolds number and later Dandy and Dwyer [10] extended it to high particle Reynolds numbers. The virtual mass and pressure gradient forces were based on the fluid acceleration and local pressure gradient, respectively [11]. A gravitational force is also applied in the vertical direction in all simulations. To account for two-way momentum coupling, for a given computational cell, the mean forces applied to each particle during the timestep are also distributed to the local fluid cell. Particle collisions are also taken into account and assumed to be elastic and obey the hard-sphere conditions when calculating rebound positions and velocities.

The Lagrangian particle tracker was developed to model large quantities of dispersed solids and runs concurrently with Nek5000. A fourth-order Runge-Kutta method was implemented to solve the particle equation of motion for each particle at every time-step. To initialise the computations, the particles were injected at a random position within the fully developed fluid flow domain and assigned the fluid velocity at that location. Particles collisions with the pipe wall were considered to be elastic. Periodic boundary conditions were applied at the extents of the streamwise direction and no-slip conditions for the wall at $r^* = 0.5$. Statistical data was gathered for the fully-coupled simulations after a few particle response times ($t^* = 20$) to allow time for the injected phase to adjust to the surrounding fluid.

2.3. Particle Deposition

Rice [12] investigated the settling and deposition behaviour of suspensions of dense particles in closed cylindrical pipes using ultrasonic methods, with the onset of particle deposition and resuspension from beds studied. In the experiments performed, a range of parameters were considered, though pipe diameter was not. Two ways of evaluating the critical deposition velocity were proposed, i.e. the velocity at which particles first start to deposit out in a flow. Both particles depositing as the flow rate was decreased, and in contrast when the particles were resuspended from the pipe floor as the flow rate was increased, were considered, arguing that these approaches were equivalent and represented different ways to obtain the same deposition velocity.

In the present study, depositing pipe flows were performed with the DNS and LPT codes at two different Stokes numbers, $St^+ = 5.55$ and 16.78. A fully developed particle-laden turbulent pipe flow at $Re_\tau = 720$ was first run, with the flow rate subsequently decreased regularly until particle deposition occurred. To achieve this, the pressure gradient along the pipe was lowered by two per cent every 2000 timesteps ($t^* = 2$). The dispersion function and mean displacement of the particles were also monitored, with the dispersion function, $D^*_{y(t)}$, defined as:

$$D^*_{y(t)} = \left(\sum_{i=1}^{N_p} \frac{(y^*_{i(t)} - y^*_{m(t)})^2}{N_p} \right)^{1/2} \tag{5}$$

Here, $y^*_{i(t)}$ is the particle displacement in the vertical direction, $y^*_{m(t)}$ the mean vertical particle position, sampled across the entire domain, and N_p the total number of particles [13]. Table 2 shows the configuration of the depositing pipe flows. In both cases, the same concentration, particle diameter and number of particles were used. It should be noted that the maximum value of ϕ found in regions outside the deposition zone considered below was 2.5×10^{-3}.

Table 2. Particle phase parameters.

Parameter	Shear Reynolds number, $Re_\tau = 720$	
	$St^+ \cong 5.55$	$St^+ \cong 16.78$
Particle diameter, d_p^*	0.005	0.005
Axial length	12.5D	12.5D
Number of particles, N_p	105k	105k
Bulk Stokes number, St_b	0.125	0.379
Density ratio, ρ_p^*	7.71	23.3
Volume fraction, ϕ	0.0007	0.0007
Particle timestep, Δt^*	0.001	0.001

3. RESULTS AND DISCUSSION

3.1. Single-Phase Flow Validation

Single-phase simulations were performed at shear Reynolds numbers of $Re_\tau = 277$ and $Re_\tau = 720$ in order to validate the DNS approach being used. In each simulation, statistical data were gathered for analysis. The simulation results were compared with various DNS and experimental datasets available in the literature at, or approximately equal to, the Reynolds numbers of the simulations performed. For each simulation the mean velocity profiles, and the root mean square of the velocity fluctuations and shear stress, were compared. Only literature data with incompressible and Newtonian fluid flows was used for validation and, where possible, multiple experiments and DNS datasets were compared with the current simulations.

Figure 2 shows the axial mean velocity profile of the present predictions at a shear Reynolds number $Re_\tau = 720$, and compares this with the DNS results of El Khoury [14] at $Re_\tau = 720$ and Singh et al. [15] at $Re_\tau \approx 640$. The present work agrees with the results of El Khoury [14] but slightly deviates when contrasted with Singh et al. [15], likely due to the difference in Reynolds number. The results are additionally compared with the den Toonder et al. [2] experimental dataset at $Re_\tau \approx 630$. These results correlate well with the present work given the difference in Reynolds number.

Figure 3 displays the axial, z^*_{rms}, radial, r^*_{rms}, azimuthal, θ^*_{rms}, normal stress profiles, and the Reynolds shear stress, $< u_z\, u_r >^*$, at $Re_\tau = 720$ showing good agreement with El Khoury [14], Singh et al. [15], and den Toonder et al [2]. On the pipe centreline, all the simulations and experimental data are in good agreement with the inner scaled profiles of the present DNS. Overall, comparison of the normal and shear stresses, as a function of $0.5 - r^*$, gives confidence in the present continuous phase predictions. Similar agreement with literature data was also found for the $Re_\tau = 277$ case considered.

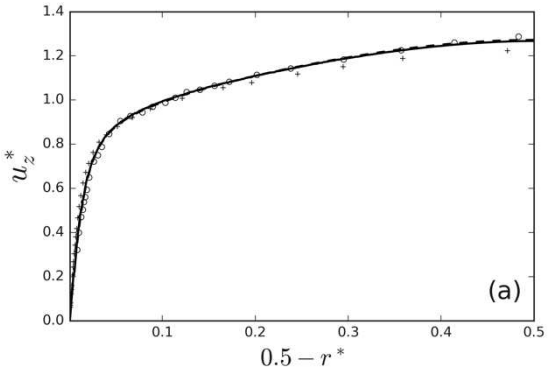

Figure 2. Mean axial velocity u_z^* : — present DNS at $Re_\tau = 720$; − − El Khoury (2013) DNS at $Re_\tau = 720$; + Singh et al. (2018) DNS at $Re_\tau \approx 640$; ○ den Toonder et al. (1997) experiments at $Re_\tau \approx 630$.

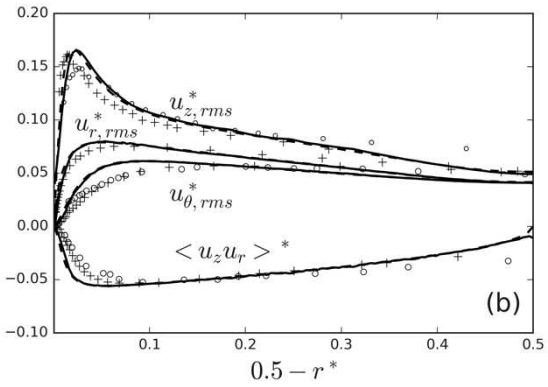

Figure 3. Axial, z^*_{rms}, radial, r^*_{rms}, and azimuthal, θ^*_{rms}, normal stresses and Reynolds shear stress, $< u_z\, u_r >^*$: — present DNS at $Re_\tau = 720$; − − El Khoury (2013) DNS at $Re_\tau = 720$; + Singh et al. (2018) DNS at $Re_\tau \approx 640$; ○ den Toonder et al. (1997) experiments at $Re_\tau \approx 630$.

3.2. Multi-Phase Flow Validation

To validate the coupled DNS and LPT solver, a separate simulation was performed, again at $Re_\tau = 277$, and compared directly with the DNS results of Vreman [16] who considered the dispersion glass-beads. In the present work, the particles were injected at random locations within the computational domain, taking the fluid velocity at their location at the start of the particle simulation. 29,400 particles were injected having a diameter of 60 μm. To best represent the parameters used in the validation case considered,

only drag and gravitational forces were used when calculating the particle trajectories, with the impact of lift considered negligible. The gravitational force was also applied in the mean flow direction, in line with [16]. The only difference was that in the present simulation a much larger number of numerical grid nodes were used. One-way and four-way coupled simulations with the same particle size and number were performed, with mean and fluctuating velocity profiles analysed.

The particle mean velocity profile and stresses are compared with the results of Vreman [16] in Figure 4. Clearly the present one-way coupled simulations are significantly different from those using four-way coupling, with the latter required to simulate the impact of particles on the continuous flow field. There is reasonable agreement with the four-way DNS predictions of Vreman [16], although some differences do occur, this likely being due to significantly increased numerical resolution used in the present work (18.7M nodes as opposed to 607k).

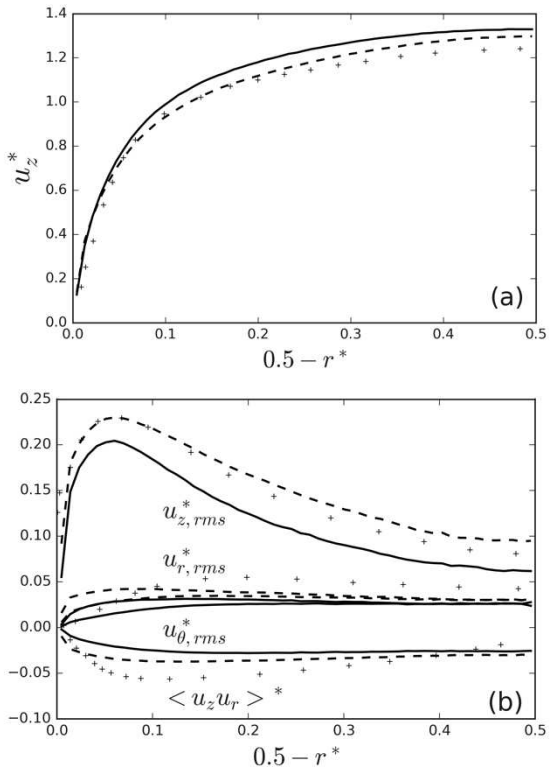

Figure 4. (a) Mean axial velocity and (b) normal and shear stresses at $Re_\tau = 277$: — present DNS one-way coupled; --- present DNS four-way coupled; + Vreman (2007) DNS four-way coupled.

3.3. Particle Deposition

The fully developed $Re_\tau = 720$ flow was used to simulate one- and four-way coupled flows at two different particle Stokes numbers of $St^+ = 5.55$ and 16.78. In both cases, the same particle volume fraction was used; 7×10^{-4}. To initialise the simulations, 105k particles were randomly injected throughout the computational domain and assigned the local interpolated fluid velocity. 50 μm particles with a density ratio (with the fluid) of 7.71 for $St^+ \cong 5.55$ and 23.3 for $St^+ \cong 16.78$ were employed.

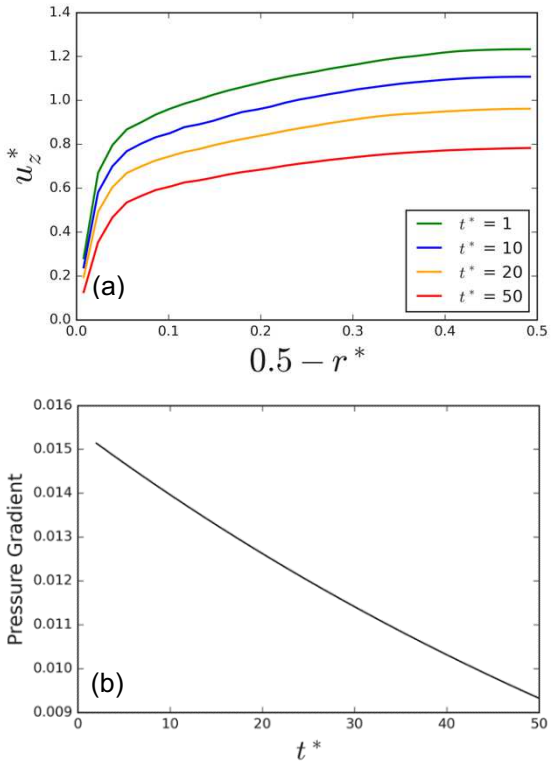

Figure 5. (a) Mean axial velocity at different t^* and (b) prescribed pressure gradient.

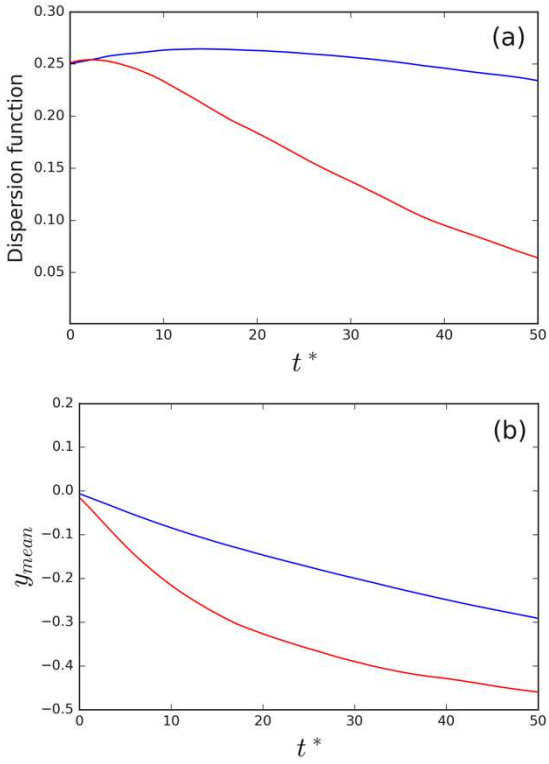

Figure 6. (a) Dispersion function in vertical direction and (b) mean vertical position of particles: blue St^+=5.55; red St^+=16.78.

Figure 5 shows the mean streamwise velocity profile and the non-dimensionalised pressure gradient reduction with time, with the latter used to drive the reduction in mass flow through the pipe in order to encourage particle deposition.

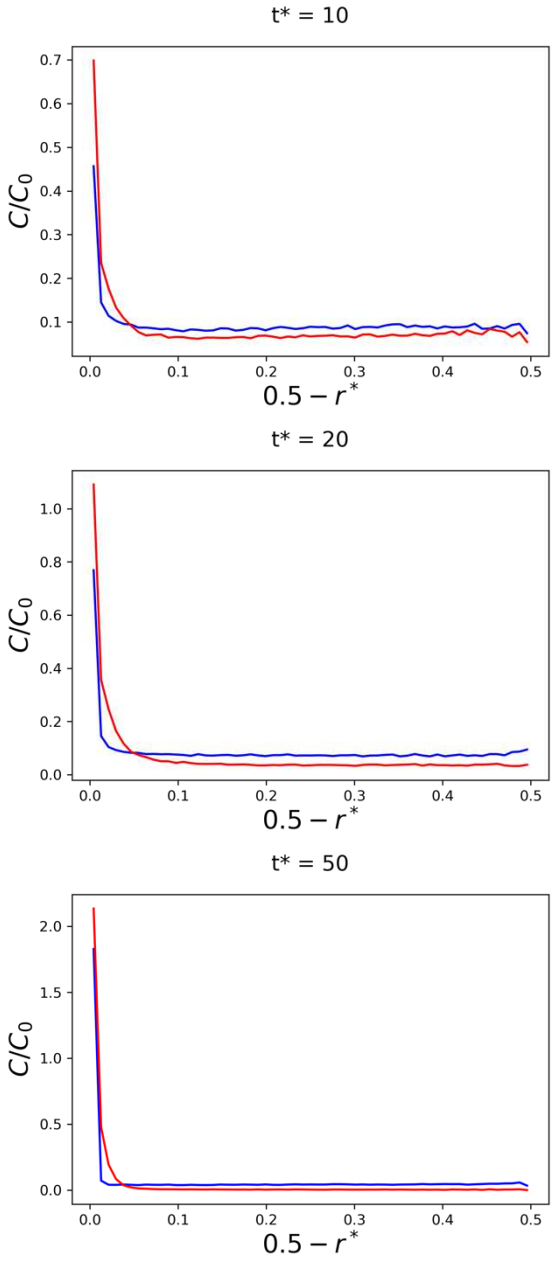

Figure 7. Mean particle concentration of $St^+ = 5.55$ (blue) and $St^+ = 16.78$ (red) particles with time, normalised by initial concentration.

Figure 6 shows the dispersion function, defined in Eq. (5), and the mean vertical position of the particles with time. At the high Stokes number, $St^+ = 16.78$, the particle dispersion and their mean vertical position decrease considerably faster with time than for the lower Stokes number case. This is due to the increased gravitational force causing the particles to accelerate in the negative vertical direction at an increased rate. For the same sized particles of $St^+ \cong 5.55$, the rate of migration towards the lower half of the pipe is much slower when compared to the $St^+ \cong 16.78$ case.

Figure 7 shows mean particle concentration profiles in the vertical direction for both particles cases at various points in time, with the concentration normalised by the initially injected concentration, C_0. The particles are seen to migrate towards the wall region and to ultimately deposit on the bottom of the pipe, with the near-wall concentration of the $St^+ = 16.78$ particles higher than for the lower Stokes number case. This can be seen more clearly in Figs. 8 and 9, which plot the positions of particles close to the wall ($0.49 \leq r^* \leq 0.5$) in the lower half of the pipe with time. Initially, the particles are relatively evenly distributed within the domain, but with increasing time migration to the lower regions of the pipe occurs and for the high Stokes number case by $t^* = 50$ a particle bed appears to have formed. In contrast, for the lower Stokes number case a bed is not formed, although the majority of the particles have migrated towards the bottom of the pipe and formed dune-like structures. These observations are in-line with the calculated dispersion function and mean particle position values given in Fig. 6, where from approximately $t^* = 5$ the higher Stokes number particles start to deviate from the lower Stokes number case, and as time increases particle deposition proceeds at a significantly higher rate.

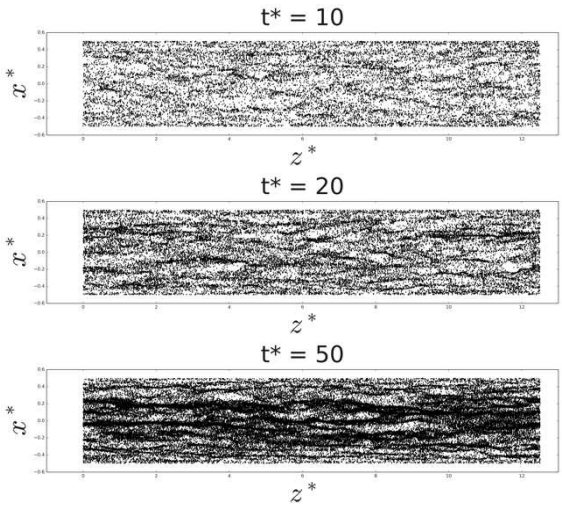

Figure 8. Instantaneous plots of particle position in the near-wall region of the lower half of the pipe for $St^+ \cong 5.55$.

To further examine the local behaviour of the particles, probability density function information on particle properties was also gathered. Figure 10 first shows PDFs for both Stokes number particles for the particle velocity in the vertical direction which illustrates a larger spread of negative vertical velocities for the low Stokes particles. There also exists a slight skew towards negative velocities in both

cases due to the influence of gravity. Secondly, PDFs of the particles' streamwise velocity are given, where for the low Stokes number particles two regimes are observed, with some particles possessing low speeds (those trapped in the wall region) or higher speeds (those in the bulk of the flow). The high Stokes number particles do not exhibit this behaviour, with the majority of particles existing at low velocities due to their proximity to the lower wall of the pipe, underlining the importance of flow and particle interactions within the wall-region such as particle preferential concentration in low speed streaks (seen in Figs. 8 and 9), and particle interaction with near-wall turbulence structures which, through sweep and ejection events, modulate the particle flux towards the wall. PDFs of the slip velocity are also given in Fig. 10 which tend to increase as the Stokes number increases, as would be expected for the more inertial particles. Lastly, PDFs of the vertical position of the particles is considered, with the high Stokes particles occupying much greater negative positions, in line with previous observations.

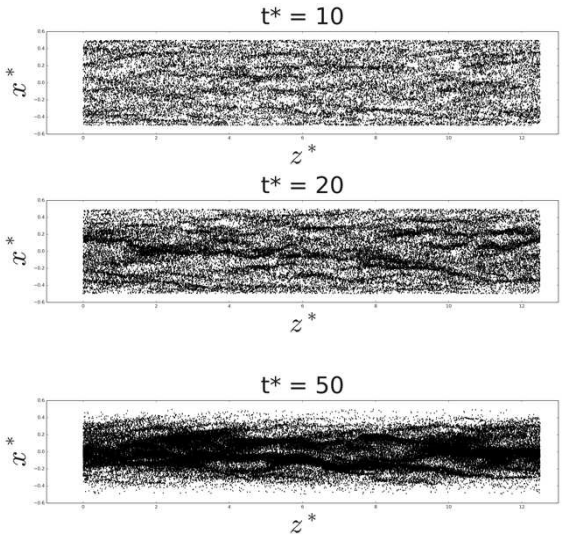

Figure 9. Instantaneous plots of particle position in the near-wall region of the lower half of the pipe for $St^+ \cong 16.78$.

4. CONCLUSIONS

This study has considered the effect of particle Stokes number on particle deposition within a wall-bounded turbulent flow. Direct numerical simulations have been carried out, coupled with Lagrangian particle tracking, for fully developed turbulent pipe flows, with mean velocity, and normal and shear stress, profiles within single-phase flows in agreement with other simulation results in the literature and experimental datasets. A similar validation for particle-laden flows has also been performed, again with good agreement with alternative simulations found.

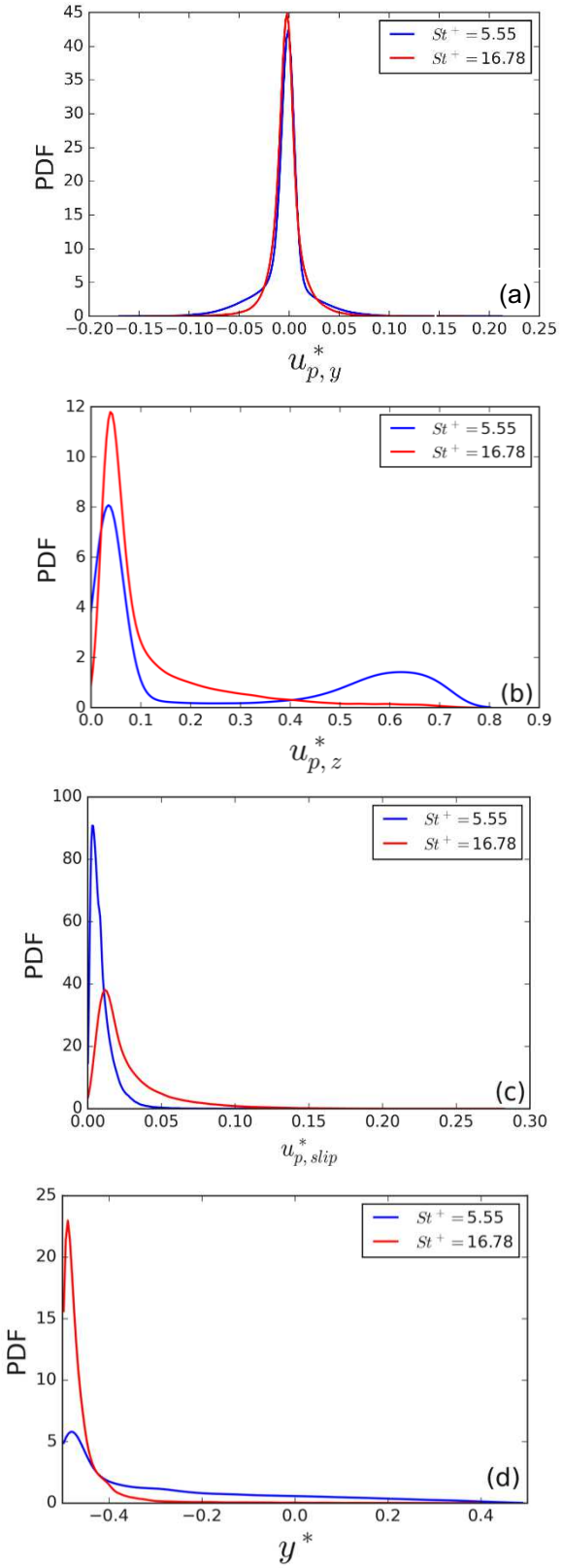

Figure 10. Probability density functions for $St^+ \cong 5.55$ and 16.78 particles at t^*=50: (a) vertical velocity; (b) streamwise velocity; (c) slip velocity; (d) vertical position.

A fully developed $Re_\tau = 720$ pipe flow has been used to perform four-way coupled simulations to

predict particle deposition. These were performed at two different particles Stokes numbers, $St^+ \cong 5.55$ and 16.78. The pressure gradient along the pipe was lowered with time and the gravitational force was applied in the vertical direction. The conveying flow rate then decreased allowing particle deposition to occur.

From the analysis performed, it can be concluded that particle deposition is very sensitive to Stokes number. The determined particle dispersion function and particle mean displacement have been demonstrated to decrease considerably faster with time at higher Stokes numbers due to the increased gravitational force acting on the particles. Particle concentrations demonstrate particle migration towards the lower wall regions and ultimately to deposition on the bottom of the pipe, with a particle bed forming for the higher Stokes number case. In contrast, at lower Stokes number, a bed is not formed, although the majority of the particles do form dune-like structures on the base of the pipe. Lastly, an analysis of the particle dynamics, carried out by examining probability density functions of particle velocities and positions, confirms the above findings.

Further work will examine a wider range of particle Stokes numbers and compare particle deposition velocities derived from the simulations with those obtained experimentally from both particle deposition and resuspension approaches to determining this parameter.

ACKNOWLEDGEMENTS

The authors are grateful for funding from the UK Engineering and Physical Sciences Research Council and the University of Leeds through the TRANSCEND (Transformative Science and Engineering for Nuclear Decommissioning) project (EP/S01019X/1).

REFERENCES

[1] Guha, D., Ramachandran, P. A., Dudukovic, M. P., 2007, "Flow field of suspended solids in a stirred tank reactor by Lagrangian tracking." *Chemical Engineering Science*, Vol. 62, pp. 6143-6154.

[2] den Toonder, J. M. J., Hulsen, M. A., Kuiken, G. D. C., Nieuwstadt, F. T. M., 1996, "Drag reduction by polymer additives in a turbulent pipe flow: Numerical and laboratory experiments." *Journal of Fluid Mechanics*, Vol. 337, pp. 1193-231.

[3] Fischer, P. F., Lottes, J. W., Kerkemeier, S. G., 2008, Nek5000, see http://nek5000.mcs.anl.gov (accessed 12th November 2021).

[4] Patera, A.T., 1984, "A spectral element method for fluid dynamics: Laminar flow in a channel expansion." *Journal of Computational Physics*, Vol. 54, pp. 468-488.

[5] Maday, Y., Patera, A. T., 1989, "Spectral element methods for the incompressible Navier-Stokes equations." In: *State-of-the-Art Surveys on Computational Mechanics*, pp. 71-143.

[6] Maxey, M. R., Riley, J. J., 1983, "Equation of motion for a small rigid sphere in a nonuniform flow." *Physics of Fluids*, Vol. 26, pp. 883-889.

[7] Mortimer, L. F., Njobuenwu, D. O., Fairweather, M., 2019, "Near-wall dynamics of inertial particles in dilute turbulent channel flows." *Physics of Fluids*, Vol. 31, 063302.

[8] Schiller, L., 1934, "Neue quantitative versuche zur turbulenzentstehung." *ZAMM-Journal of Applied Mathematics and Mechanics*, Vol. 14, pp. 36-42.

[9] Saffman, P., 1965, "The lift on a small sphere in a slow shear flow." *Journal of Fluid Mechanics*, Vol. 22, pp. 385-400.

[10] Dandy, D. S., Dwyer, H.A., 1990, "A sphere in shear flow at finite Reynolds number: Effect of shear on particle lift, drag, and heat transfer." *Journal of Fluid Mechanics*, Vol. 216, pp. 381-410.

[11] Stokes, G. G., 1851, "On the effect of the internal friction of fluids on the motion of pendulums." *Transaction of the Cambridge Philosophical Society*, Vol. 9, pp. 8-106.

[12] Rice, H. P., 2013, "Transport and deposition behaviour of model slurries in closed pipe flow." *PhD Thesis, University of Leeds*.

[13] Fairweather, M., Yao, J., 2009, "Mechanisms of particle dispersion in a turbulent, square duct flow." *AIChE Journal*, Vol. 55, pp.1667-1679.

[14] El Khoury, G. S., 2013, "Direct numerical simulation of turbulent pipe flow at moderately high Reynolds numbers." *Flow Turbulence and Combustion*, Vol. 91, pp. 475-495.

[15] Singh, J., Rudman, M., Blackburn, H.M., 2018, "Reynolds number effects in pipe flow turbulence of generalized Newtonian fluids." *Physical Review Fluids*, Vol. 3, 094607.

[16] Vreman, A. W., 2007, "Turbulence characteristics of particle-laden pipe flow." *Journal of Fluid Mechanics*, Vol. 584, pp. 235-279.